Applied Acoustics 213 (2023) 109654

Contents lists available at ScienceDirect

Applied Acoustics

journal homepage: www.elsevier.com/locate/apacoust

Modelling the sound absorption of panels with tapered elliptic micro-perforations

M.L. Fung [a], S.K. Tang [b,*], M. Leung [c]

[a] Department of Building Environment and Energy Engineering, The Hong Kong Polytechnic University, Hong Kong, China
[b] School of Engineering, The University of Hull, Hull HU6 7RX, United Kingdom
[c] Architectural Acoustics (International) Limited, Hong Kong Special Administration Region, China

ARTICLE INFO

Keywords:
Sound absorption
Microperforation

ABSTRACT

A theoretical model is developed in the present study to predict the spectral characteristics of the sound absorption of solid panels with tapered elliptic micro-perforations backed by a rigid wall cavity. In the model, plane wave propagation is assumed along the length of the perforation in the presence of a viscous boundary layer at the internal wall of the perforation. End impedances are approximated using results in existing literature. Validation is done using impedance tube measurements. It is confirmed that the present tapered elliptic perforation model can give much better agreement with experimental results than the conventional cylindrical perforation model for all micro-perforation configurations tested. Results also suggest the importance of perforation density in controlling the variation of sound absorption of the panel absorbers upon changes in perforation configurations.

1. Introduction

The theory of micro-perforated sound absorbing panels (MPP) was first introduced by Maa [1,2] in the 90 s. This type of sound absorbers is featured by the many sub-millimetre diameter perforations on a solid panel backed by a rigid cavity. With the right configuration, the MPP absorbers can give much better low frequency sound attenuation than the conventional fibrous sound absorption of similar thickness [3]. As the commonly used fibrous sound absorption materials will degenerate gradually into tiny respirable fibres, which can suspend in air and are hazardous to human health, the MPP absorbers have attracted great attention of building professionals, engineers and academics in the past few decades. Commercial MPP absorbers are now available.

The strong potential of the MPP absorbers as a next generation sound absorber [4] has sparked off significant worldwide research effort into its physics, applications and performance improvements. Typical examples include the parametric studies of Liu et al. [5], Bravo et al. [6] and Sakagami et al. [7], the multilayer MPPs of Sakagami et al. [8], Bravo et al. [9] and Cobo and Simón [10]. Wang et al. [11] investigated the effect of the backing cavity on the performance of the MPP absorbers, while Wang and Huang [12] studied the possible improvement of sound attenuation by coupling MPPs which are backed by cavities of different dimensions. There are also investigations into the use of MPP for flow duct silencing [13,14] and in the construction of acoustic metamaterials [15]. However, this list is by no mean exhaustive.

The perforations are assumed to be cylindrical in most of the MPP studies. While this could be true if the perforations are created by individual drilling, this is not generally the case in practice for fast and cost-effectiveness manufacture. Based on the results of Stinson [16], Ning et al. [17] developed formulae for the acoustic impedance of triangular and square un-tapered perforations. That of micro slot perforation was also given. In recent years for light-weight applications, MPPs can be made of acrylic (PMMA) and the perforations are produced using the laser punching technique. The perforations are no longer circular, but elliptic.

Fig. 1 illustrates some typical examples of the finishing of laser punched perforations. The geometry of the perforations depends on laser punching setting (laser power W, duration of single punching t_l, laser focus height from the acrylic panel front surface f_h) and the thickness of the acrylic panel h. Since the front surface of the panel receives the laser for a longer period of time, there is more acrylic material melting on the front surface than the bottom surface. The perforations are therefore tapered as shown in Fig. 1. Also, the perforation edges are not sharp. A dome-like smoothed edge is usually found at the bottom

* Corresponding author.
E-mail address: S.Tang@hull.ac.uk (S.K. Tang).

https://doi.org/10.1016/j.apacoust.2023.109654
Received 19 July 2023; Received in revised form 26 August 2023; Accepted 13 September 2023
Available online 17 September 2023

surface of the perforation. This tends to reduce the magnitude of the exit acoustic impedance [18]. The practical configuration of the micro-perforation deviates very much from cylindrical. The Maa's model [1,2] has become much less realistic. Improvement is needed. The study of tapered micro-perforations is very rarely found in existing literature. Observing that the diameter of the micro-perforation is very small compared to the wavelength of the sound to be attenuated, Herdtle et al. [19] uses the technique of incompressible and isothermal computational fluid dynamics to understand the transfer impedances of tapered cylindrical holes, but it appears that some parameters in their model are obtained by empirical method.

To predict the MPP sound absorption performance, we analyse in the present study the sound propagation across a short elliptic duct in the presence of a viscous wall boundary layer in the first place. Plane waves are assumed to propagate across the tapered elliptic duct. Experimental measurements using the standard impedance tube method have been carried out to validate the theoretical model, followed by a discussion on the effects of panel thickness and the eccentricity difference between the two sides of the perforation on the sound absorption performance of the MPP absorbers.

2. Theoretical model for sound propagation along elliptic tubes

For a straight tube of length h (i.e. the thickness of the MPP) and equivalent diameter much smaller than the wavelength of the sound which propagates across it, all circumferential variations within the tube vanish and the incompressible approximation is valid. For a small velocity perturbation u, the corresponding flow equation is

$$\frac{\partial u}{\partial t} = -\frac{1}{\rho_o}\nabla p + \frac{\mu}{\rho_o}\nabla^2 u, \tag{1}$$

where p is the pressure fluctuation, μ the coefficient of viscosity of the fluid in concern, ρ_o the fluid density and t the time [20]. An elliptic cross section with major and minor axis lengths 2α and 2β is characterized by the focus separation $2a$ and two variables σ and τ (Fig. 2) with

$$0 \le \tau \le 2\pi, 0 \le \sigma \le \sigma_o, a = \sqrt{\alpha^2 - \beta^2} \text{and} \tanh(\sigma_o) = \beta/\alpha. \tag{2}$$

Transforming Eq. (1) into elliptic coordinate system, one obtains

$$\rho_o \frac{\partial u}{\partial t} = -\frac{\partial p}{\partial z} + \mu\left[\frac{1}{a^2(\sinh^2\sigma + \sin^2\tau)}\left(\frac{\partial^2 u}{\partial\sigma^2} + \frac{\partial^2 u}{\partial\tau^2}\right) + \frac{\partial^2 u}{\partial z^2}\right]$$
$$\approx \frac{\Delta p}{h} + \frac{\mu}{a^2(\sinh^2\sigma + \sin^2\tau)}\left(\frac{\partial^2 u}{\partial\sigma^2} + \frac{\partial^2 u}{\partial\tau^2}\right), \tag{3}$$

where Δp is the pressure drop across the tube and u does not vary with z. For a sinusoidal time varying u, Eq. (3) becomes

$$\frac{j\rho_o\omega a^2}{2\mu}u - \frac{1}{(\cosh 2\sigma - \cos 2\tau)}\left(\frac{\partial^2 u}{\partial\sigma^2} + \frac{\partial^2 u}{\partial\tau^2}\right) = a^2\frac{\Delta p}{2\mu h}, \tag{4}$$

where $j = \sqrt{-1}$. The general solution of Eq. (4) can be obtained by the method of separation of variables, and its particular solution is simply

$$u = \frac{\Delta p}{j\rho_o\omega h}. \tag{5}$$

The solution of Eq. (4) is, after some algebra,

$$u = \sum_{n=0}^{\infty}(A_n Ce_n(\sigma, q) + B_n Se_n(\sigma, q))(C_n ce_n(\tau, q) + D_n se_n(\tau, q)) + \frac{\Delta p}{j\rho_o\omega h}, \tag{6}$$

where $q = -j\rho_o\omega a^2/4\mu$, ce_n and se_n the angular Mathieu functions of the first kind of integer order n [21], Ce_n and Se_n the modified radial Mathieu functions of the first kind of integer order n [21] and A_n, B_n, C_n, and D_n, are constants to be determined. The symmetry of u requires

$$u(\sigma, \tau) = u(\sigma, \pi - \tau) = u(\sigma, \pi + \tau) = u(\sigma, 2\pi - \tau) \tag{7}$$

such that u cannot have a period of 2π. The quantities with odd n order in Eq. (6) are thus irrelevant. Parity of u must also be even and thus the solution (Eq. (6)) can be reduced to

$$u = \sum_{n=0}^{\infty}\left[A'_{2n} Ce_{2n}(\sigma, q) ce_{2n}(\tau, q) + B'_{2n} Se_{2n}(\sigma, q) se_{2n}(\tau, q)\right] + \frac{\Delta p}{j\rho_o\omega h}. \tag{8}$$

Further, since u is symmetrical about the interfoci line (x-axis) and is continuous and differentiable at $\sigma = 0$, $B'_{2n} = 0$. The final solution is thus

$$u = \sum_{n=0}^{\infty} A'_{2n} Ce_{2n}(\sigma, q) ce_{2n}(\tau, q) + \frac{\Delta p}{j\rho_o\omega h}. \tag{9}$$

The 'no-slip' wall condition in the presence of the viscous boundary layer requires that $u(\sigma_o, \tau) = 0$,

$$u(\sigma_o, \tau) = \sum_{n=0}^{\infty} A'_{2n} Ce_{2n}(\sigma_o, q) ce_{2n}(\tau, q) + \frac{\Delta p}{j\rho_o\omega h} = 0. \tag{10}$$

Expressing ce_{2n} in the form of a Fourier series [21],

$$ce_{2n}(\tau, q) = \sum_{r=0}^{\infty} A_{2r}^{(2n)}(q)\cos(2r\tau), \tag{11}$$

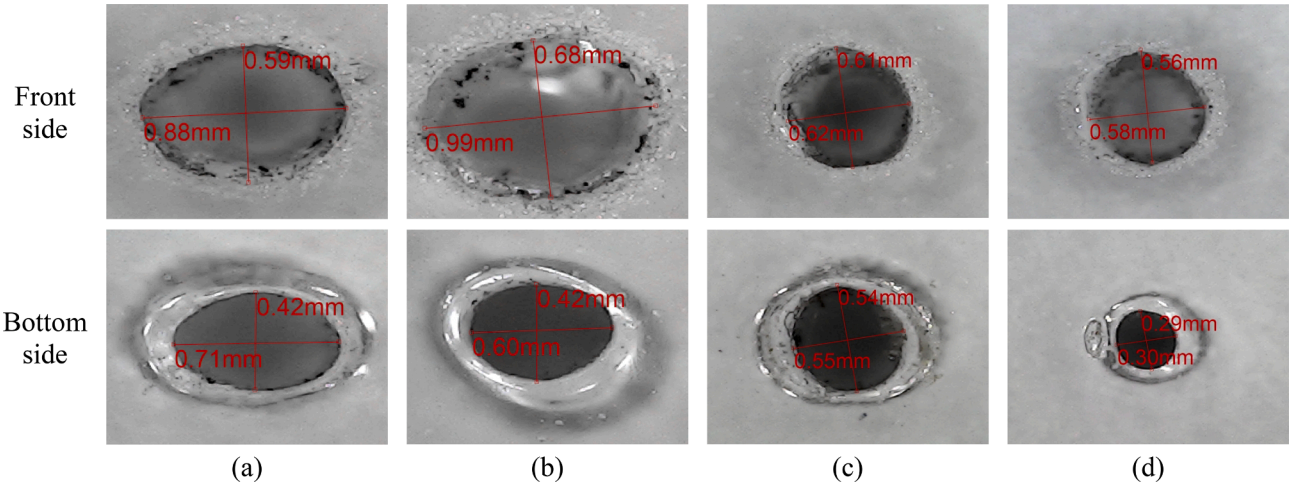

Fig. 1. Examples of elliptic perforation created by laser punching on acrylic panel. (A). $h = 1.5$ mm, $f_h = 6$ mm, $W = 82.5$ W, $t_l = 100$ msec;(b) $h = 3$ mm, $f_h = 6$ mm, $W = 82.5$ W, $t_l = 100$ msec; (c) $h = 1$ mm, $f_h = 4$ mm, $W = 82.5$ W, $t_l = 80$ msec; (d) $h = 1$ mm, $f_h = 6$ mm, $W = 27.5$ W, $t_l = 100$ msec.

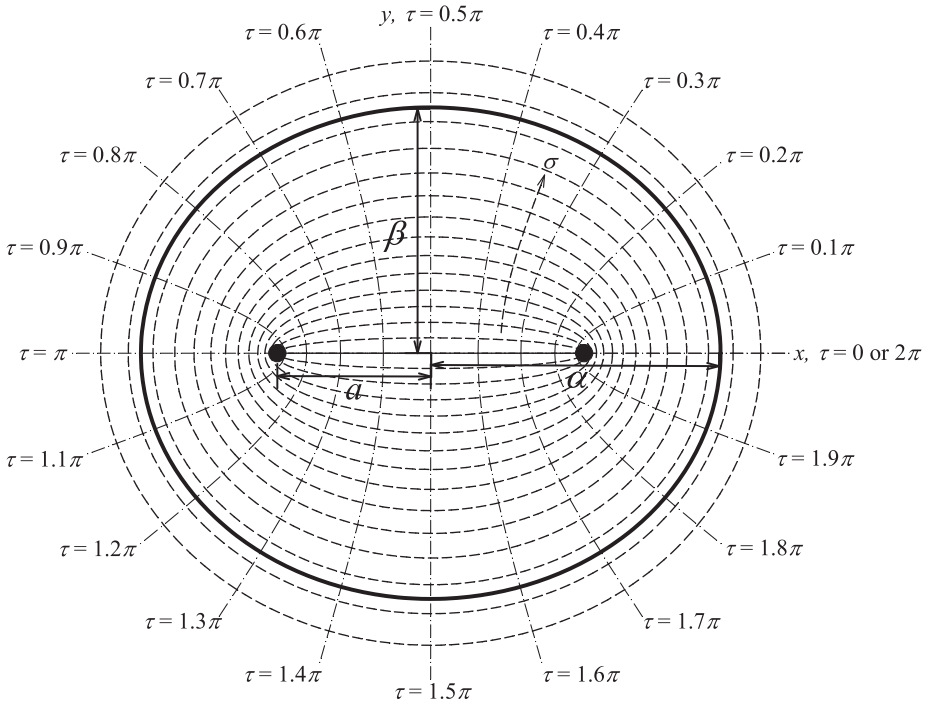

Fig. 2. Elliptic co-ordinate and nomenclature. ———: An ellipse; — · —: τ; – – – –: σ; ●: foci.

where $A_{2r}^{(2n)}$ s are complex functions of q and with the recurrence relationships of these functions (see for instance, Ref. 21), one can write, for any integer value of r,

$$A_{2r}^{(2n)}(q) = A_0^{(2n)}(q) f_{2r}(n,r,q), \tag{12}$$

where f_{2r} is a complex function of n, r and q. One can then obtain that

$$\int_0^{2\pi} ce_{2n}(\tau,q)d\tau = 2\pi A_0^{(2n)}(q) \text{and} \int_0^{2\pi} ce_{2n}^2(\tau,q)d\tau = \pi\left[A_0^{(2n)}(q)\right]^2 F_{2n}(n,q), \tag{13}$$

where

$$F_{2n}(n,q) = 2 + \sum_{r=1}^{\infty} [f_{2r}(n,r,q)]^2. \tag{14}$$

Then, it is straight-forward to show that

$$A_{2n}^{'} = -\frac{2}{Ce_{2n}(\sigma_o,q)A_0^{(2n)}(q)F_{2n}(n,q)} \frac{\Delta p}{j\rho_o\omega h}. \tag{15}$$

The cross sectional area of the tube A is

$$A = \frac{a^2}{2}\int_0^{2\pi}\int_0^{\sigma_o} (\cosh 2\sigma - \cos 2\tau)d\sigma d\tau = \pi a^2 \int_0^{\sigma_o} \cosh 2\sigma d\sigma = \frac{\pi a^2}{2}\sinh 2\sigma_o = \pi\alpha\beta. \tag{16}$$

The mean velocity $\bar{u}$ over the elliptic tube cross section is thus

$$\bar{u} = \frac{1}{2A}\int_0^{2\pi}\int_0^{\sigma_o} ua^2(\cosh 2\sigma - \cos 2\tau)d\sigma d\tau, \tag{17}$$

One can show by substituting Eqs. (9), (15) and (16) into Eq. (17) that the specific acoustic impedance

$$Z = \frac{\Delta p}{\bar{u}} = j\rho_o\omega h\left[1 - \frac{2}{\sinh 2\sigma_o}\int_0^{\sigma_o}\sum_{n=0}^{\infty}\frac{Ce_{2n}(\sigma,q)}{Ce_{2n}(\sigma_o,q)F_{2n}(n,q)}\left(2\cosh 2\sigma - \frac{n}{q}\right)d\sigma\right]^{-1}. \tag{18}$$

When $\alpha \to \beta$, that is when the perforation cross-section becomes very circular, $\sigma_o \to \infty$ and $q \to 0$. It is shown in Fig. 3 that the predictions by Eq. (18) agree very well with those obtained by using the formula of Maa [1,2], though there is a negligibly small derivation of the resistance terms. Solving Eq. (18) analytically with $\sigma_o \to \infty$ and $q \to 0$ is very tedious. Thus, only numerical calculation is adopted in the comparison.

The use of the above analytical approach to estimate the acoustic impedance is very hard when the tube is tapered. Herdtle et al. [19] used incompressible computational fluid dynamics in their analysis of the tapered circular hole acoustic impedance. Empirical constants were proposed. Though this method is in general applicable to the case of an elliptic hole, it is not practical as there can be many combinations of α and β, apart from the degree of tapering and h.

During the manufacturing process, the laser beam is normal to the acrylic panel and thus the axis of the perforation is normal to the panel as well. The cross section of the perforation varies along the length of the tapered perforation. For simplicity, we assume both α and β vary linearly with z:

$$\alpha = \alpha_f - \frac{\alpha_f - \alpha_b}{h}z \text{ and } \beta = \beta_f - \frac{\beta_f - \beta_b}{h}z, \tag{19}$$

where the suffices f and b hereinafter denote quantities associated with the front ($z = 0$) and bottom ($z = h$) side of the perforation respectively. The separation between the two foci $2a$, the cross-section area A and σ_o are thus also functions of z.

To analyze the sound propagation along the tapered elliptic perforation, the whole perforation is divided into infinite number of thin elliptic slices of infinitesimal width Δz and plane wave propagation is assumed within each of them. The pressure drop along each tube,

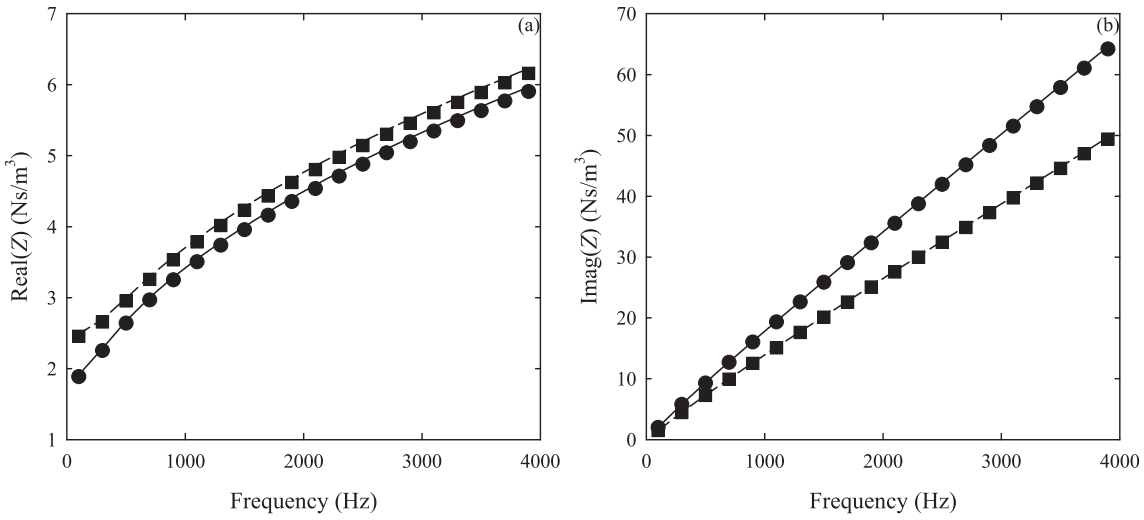

Fig. 3. The convergence of Eq. (18) to the formula of Maa [1] when $\alpha \to \beta$. (a) Resistance Real(Z); (b) reactance Imag(Z). ●: $\alpha = 0.4$ mm, $h = 2$ mm (Maa [1]); ■: $\alpha = 0.3$ mm, $h = 1.5$ mm (Maa [1]); ———: $\alpha = 0.4$ mm, $h = 2$ mm (Eq.(18)); – – – –: $\alpha = 0.3$ mm, $h = 1.5$ mm (Eq.(18)).

following Eq. (18), is

$$\delta p = j\rho_o \omega \bar{u} \Delta z \left[1 - \frac{2}{\sinh 2\sigma_o} \int_0^{\sigma_o} \sum_{n=0}^{\infty} \frac{Ce_{2n}(\sigma, q)}{Ce_{2n}(\sigma_o, q) F_{2n}(n, q)} \left(2\cosh 2\sigma - \frac{n}{q} \right) d\sigma \right]^{-1}. \tag{20}$$

As h is very small when compared to the wavelength of the sound to be attenuated, the volumetric air flow rate, $Q\ (= A\bar{u})$, is constant along the length of the perforation. The acoustic impedance of the tapered elliptic perforation is simply $Z_t = \Delta p/Q$, where

$$\frac{\Delta p}{Q} = \int \frac{\delta p}{Q} = \int_0^h j\rho_o \omega \left[A - \pi a^2 \int_0^{\sigma_o} \sum_{n=0}^{\infty} \frac{Ce_{2n}(\sigma, q)}{Ce_{2n}(\sigma_o, q) F_{2n}(n, q)} \left(2\cosh 2\sigma - \frac{n}{q} \right) d\sigma \right]^{-1} dz. \tag{21}$$

So far, the end impedances are not added. They will be discussed in Section 3. Fig. 4 shows some comparisons between the approximation by Eq. (21) and the finite-element computation using COMSOL. The thermoviscous acoustic boundary layer effect was included in the COMSOL simulation [22]. One can observe that for the larger perforation, there are only less than 5% difference in the prediction of reactance and resistance respectively (Fig. 4a). As the magnitude of the resistance of the micro-perforation is very small compared to that of its reactance, the observed deviation of resistance does not have significant effect on the prediction of the sound absorption coefficients of the MPPs. For the case of smaller perforations shown in Fig. 4b, the difference between the two predictions is in general less ~ 2%. The agreement between the two predictions for the other perforations tested are very similar to those presented in Fig. 4 and thus are not further discussed.

Equation (21), though considers only the viscous boundary layer at the internal walls of the perforation, is sufficiently accurate for the modelling the plane wave propagation in the micro-perforation. As the COMSOL finite-element simulation result does not form a significant part of the present study, they are not discussed further.

The discontinuities and the viscous damping at the inlet and outlet of

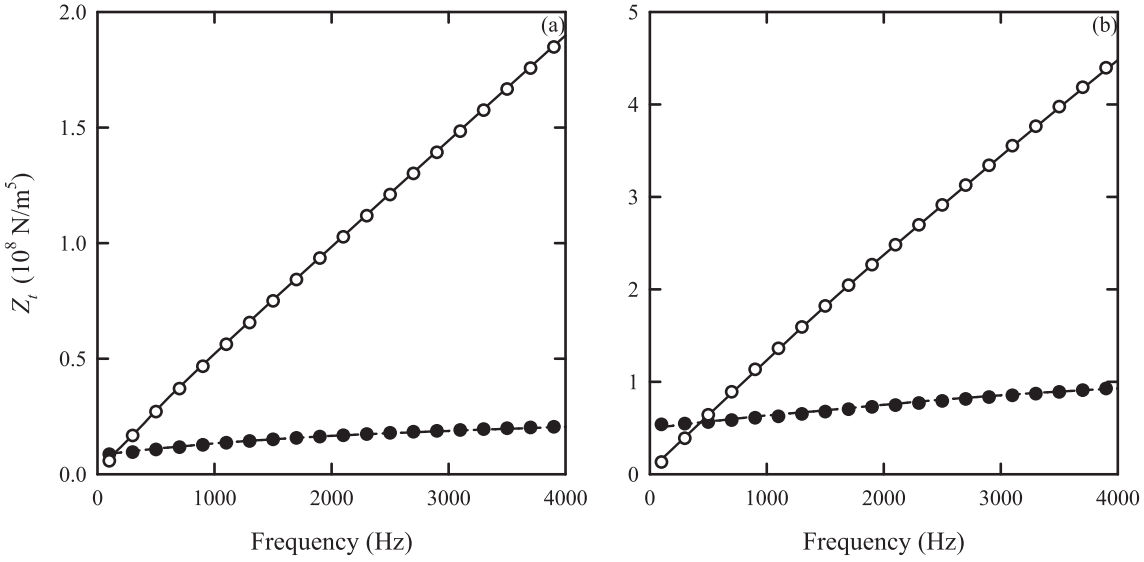

Fig. 4. Comparison between finite-element simulation and Eq. (21) predictions. (a) $\alpha_f = 0.99$ mm, $\beta_f = 0.67$ mm, $\alpha_b = 0.73$ mm, $\beta_b = 0.43$ mm, $h = 2$ mm. (b) $\alpha_f = 0.46$ mm, $\beta_f = 0.33$ mm, $\alpha_b = 0.46$ mm, $\beta_b = 0.33$ mm, $h = 1.5$ mm. ———: Imag(Z_t) by Eq.(21); – – – –: Real(Z_t) by Eq.(21); ○: Imag(Z_t) by COMSOL; ●: Real(Z_t) by COMSOL.

the micro-perforation give rise to additional inductance and resistance to the sound propagation (for instance, see Ingard [23]). Following Rayleigh [20] and with reference to the experimental observation of Ingard [23], one can approximate the additional resistance, R, at a flanged opening as

$$R = \frac{P}{A} l_d \sqrt{2\rho_o \omega \mu}, \tag{22}$$

where P is the perimeter of the opening and l_d the dissipative length correction. For an elliptic opening,

$$P = 4\alpha \int_0^{\pi/2} \sqrt{1 - e^2 \sin^2\theta}\, d\theta, \text{ and } e = \frac{\sqrt{\alpha^2 - \beta^2}}{\alpha}. \tag{23}$$

(for instance, see Abbott [24]). The additional pressure drop due to this resistance at the inlet and outlet of the perforation, Δp_r, is

$$\Delta p_r = R_f \bar{u}_f + R_b \bar{u}_b \Rightarrow \frac{\Delta p_r}{Q} = \left(\frac{P_f}{A_f^2} l_{d,f} + \frac{P_b}{A_b^2} l_{d,b} \right) \sqrt{2\rho_o \omega \mu}. \tag{24}$$

For circular inlet/outlet, l_d is equal to half the inlet/outlet radius [25]. However, the l_d for corresponding elliptic case is not yet known. For simplicity, it is taken to be half the equivalent radius in the foregoing discussions. That is, $l_d = \sqrt{\alpha\beta}/2$.

By considering the fluid loading on the plane wave at the inlet/outlet of the perforation and observing that $k\alpha \to 0$, the added mass Δm and the pressure drop due to this added mass, Δp_m, at that opening is

$$\Delta m = \rho_o A l_m \Rightarrow \Delta p_m = j\omega \rho_o l_m \bar{u}, \tag{25}$$

where l_m is the equivalent length end correction due to the added mass. According to Mechel [26],

$$\frac{l_m}{\beta} = \frac{16}{3\pi^2} \begin{cases} \left[\frac{4+\gamma^2}{8} \ln\left(\frac{16}{\gamma^2}\right) - \frac{\gamma^2}{4} \right], 0 < \gamma \le 0.641 \\ \frac{\pi}{2} \left[\frac{11+5\gamma^2}{7+9\gamma^2} \right], 0.641 < \gamma \le 1 \end{cases} \tag{26}$$

where $\gamma = \beta/\alpha$. The overall acoustic impedance of a tapered elliptic micro-perforation Z_{tap} can be obtained by combining Eqs. (20), (23) and (24):

$$Z_{tap} = Z_t + \left(\frac{P_f}{A_f^2} l_{d,f} + \frac{P_b}{A_b^2} l_{d,b} \right) \sqrt{2\rho_o \omega \mu} + j\omega \rho_o \left(\frac{l_{m,f}}{A_f} + \frac{l_{m,b}}{A_b} \right). \tag{27}$$

3. Impedance tube experiments and comparisons with theoretical models

The experiment was carried out using an impedance tube and the two-microphone method was used to estimate the specific acoustic impedances, z_{MPP}s, of the MPP absorbers. Fig. 5a and 5b show the schematics and the actual physical appearance of the experimental setup respectively. Each MPP specimen tested consisted in general of a rectangular array of tapered elliptic micro-perforations centred on the longitudinal axis of the impedance tube and was backed by a rigid wall cavity of varying length L. The effective diameter of the specimen, D, was fixed at 29 mm. There was about 1% variation in the perforation size on each specimen tested. The specific acoustic impedance of a MPP backed by a rigid cavity, normalized by ρoC, is theoretically

$$z_{MPP} = \frac{Z_{tap}}{\rho_o c n_p} - j\cot(kL), \tag{28}$$

where n_p is the number of perforations per unit area of the MPP and $k = \omega/c$ if one ignores the thermoviscous boundary layer effect at the wall of the circular cavity (for instance, see Maa [1]). The wavenumber k becomes complex after taking into account such effect [16]:

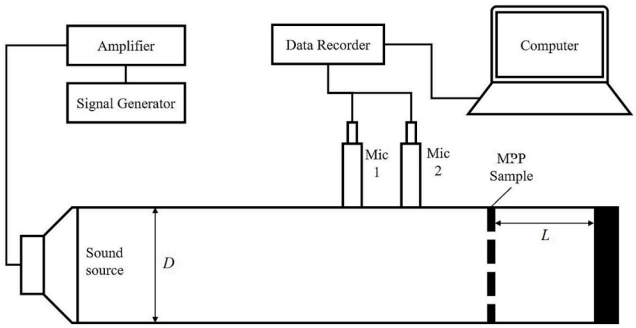

(a)

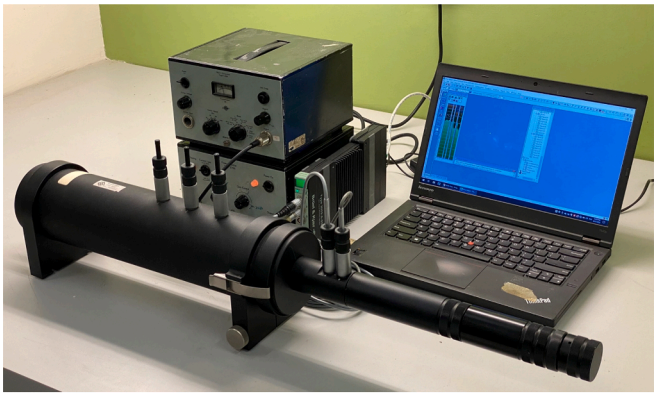

(b)

Fig. 5. Setup of the impedance tube measurement. (a) Schematics; (b) physical experimental setup.

$$k = \frac{\omega}{c} \sqrt{ \left[1 + \frac{4(\gamma_a - 1)}{D} \sqrt{\frac{j\nu}{\omega \mathrm{Pr}}} \frac{J_1\left(\frac{D}{2}\sqrt{-j\frac{\omega}{\nu}\mathrm{Pr}}\right)}{J_0\left(\frac{D}{2}\sqrt{-j\frac{\omega}{\nu}\mathrm{Pr}}\right)} \right] \Big/ \left[1 - \frac{2}{D} \sqrt{\frac{j\nu}{\omega}} \frac{J_1\left(\frac{D}{2}\sqrt{-j\frac{\omega}{\nu}}\right)}{J_0\left(\frac{D}{2}\sqrt{-j\frac{\omega}{\nu}}\right)} \right] }, \tag{29}$$

where J_0 and J_1 are the Bessel functions of the first kind with order 0 and 1 respectively, γ_a the ratio of specific heat capacities, Pr the Prandtl number and ν the kinematic viscosity of air at laboratory condition. The imaginary part of k results in a sharp peak in the resistance spectrum of the MPP absorber when $\mathrm{Re}(kL) \to \pi/2$. However, the sound absorption around this frequency is very small. The sound absorption coefficient of the MPP, α_{MPP}, is

$$\alpha_{MPP} = 1 - \left| \frac{z_{MPP} - 1}{z_{MPP} + 1} \right|^2. \tag{30}$$

The MPPs tested in the present study were of thickness (h) 1.5 mm, 2 mm and 3 mm. In this section, the experimental results will be compared with those predicted by Eqs. (28) and (30). The deficiency of prediction by assuming cylindrical perforations will also be discussed. The radius of the equivalent cylindrical perforation having the same volume as the tapered elliptic one, r_c, is

$$r_c = \sqrt{\frac{1}{h} \int_0^h \alpha\beta dz} = \sqrt{\frac{1}{6} \left[\alpha_f \beta_f + \alpha_b \beta_b + (\alpha_f + \alpha_b)(\beta_f + \beta_b) \right]}. \tag{31}$$

The formula given in Maa [1] is used to estimate the specific acoustic impedance of the MPP absorbers with the equivalent cylindrical perforations. For each perforation size, five samples of different n_p were tested (Fig. 6). For the sake of easy reference in the foregoing discussions, the MPP specimen tested are hereinafter coded as MxLyNnSz. M takes the value of 'A' or 'B'. It denotes the laser punching setting (See Table 1), x

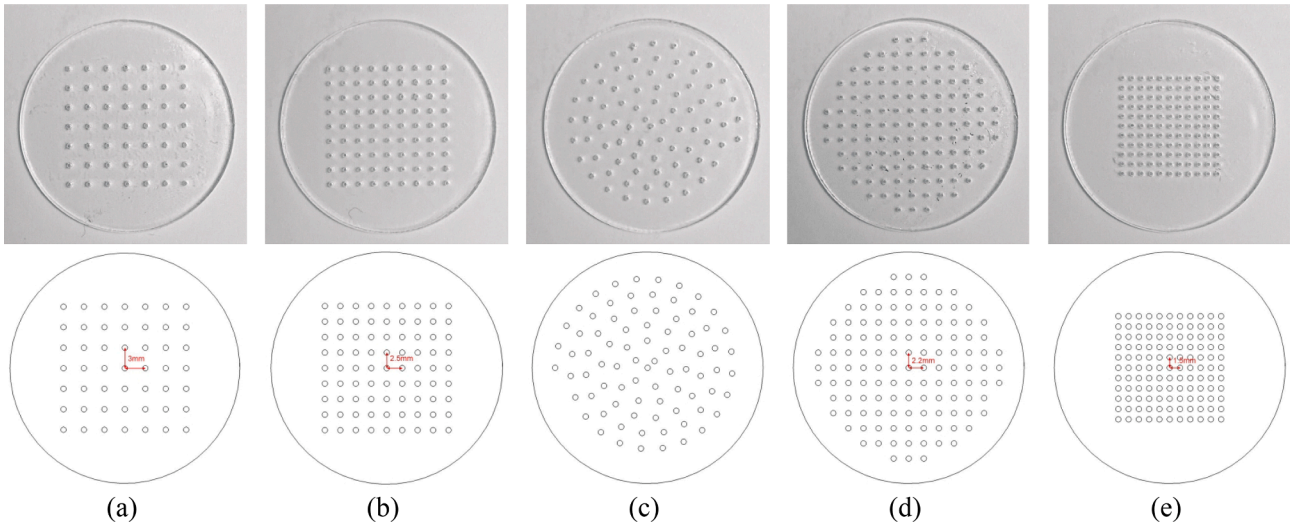

Fig. 6. The five perforation matrix configurations adopted. (a) 7 × 7 square matrix, perforation separation = 3 mm; (b) 9 × 9 square matrix, perforation separation = 2.5 mm; (c) 81 perforations, non-uniformly separated; (c) 121 perforations in rectangular matrix, perforation separation = 2.2 mm; (e) 11 × 11 square matrix, perforation separation = 1.5 mm. Upper row: physical appearance of specimens; lower row: schematics.

Table 1
Configurations of the MPPs tested (all length scales in mm).

Series	W (W)	t_l (msec)	f_h	h	α_f	β_f	$(\beta/\alpha)_f$	e_f	α_b	β_b	$(\beta/\alpha)_b$	e_b
A	82.5	100	6	1.5	0.88	0.61	0.69	0.72	0.71	0.49	0.69	0.72
				2.0	0.99	0.67	0.68	0.74	0.73	0.43	0.59	0.81
				3.0	1.00	0.68	0.68	0.73	0.60	0.41	0.68	0.73
				1.5	0.46	0.33	0.72	0.70	0.46	0.33	0.72	0.70
B	55.0	80	2	2.0	0.48	0.38	0.79	0.61	0.47	0.37	0.79	0.62
				3.0	0.49	0.38	0.78	0.63	0.44	0.30	0.68	0.73

= 10 h, y the backing cavity length L in mm, n the number of 49 (7 × 7), 81 (9 × 9) or 121 (11 × 11) which illustrates the form of the perforation matrix as well as the number of perforations on the MPP, and z 10 times the separation between perforations on the MPP in mm in general. If z is not specified, the perforation separation is non-uniform. Table 1 summarizes the approximated dimensions of the micro-perforations tested in the present study.

Fig. 7 illustrates a comparison between predictions (z_{MPP} and α_{MPP} by Eqs. (28) and (30) respectively) and experiment for the case of A15L20N49S30. The estimations by assuming equivalent cylindrical perforations are also presented. One can notice that the resistance term is very small when compared to the reactive term. Also, the predictions by present elliptic perforation model (Eqs. (28) and (30)) are much closer to the experimental results than those obtained by cylindrical perforation assumption, especially at frequencies near to that of the peak sound absorption coefficient. For an acrylic panel of thickness 1.5 mm, the coincidence frequency is around 5000 Hz. This effect is not discussed as it is not included in the present model.

The corresponding results of A15L50N49S30, which show the effect of backing cavity length on z_{MPP}, are given in Fig. 8. The longitudinal resonance within the cavity results in a dominant sharp peak on the resistance spectrum and strong reactance magnitude around the resonance frequency (Fig. 8a and 8b). However, the strong acoustic impedance at this resonance only gives rise to weak sound absorption as shown in Fig. 8c. Again, the present model gives very good predictions.

The lengthening of the backing cavity appears to have lower down the magnitude and frequency of the first sound absorption peak. The second sound absorption peak is due to the cavity which interacts with the MPP to give the resistance in z_{MPP} near to $\rho_o c$ and a small absorber reactance. This happens at a frequency just above that of the longitudinal resonance. This second peak has been observed in existing literature, for instance Wang and Huang [12], and thus is not further discussed. Structural vibration and damping, which have not been considered in the present study, could be the reason for the underestimation of the resistance term in z_{MPP}. However, this damping effect depends on the actual size of the MPP which varies widely in practice. The more important task is thus to model accurately the acoustic impedance of the perforations themselves. The structural vibration and damping effect can be added in at a later stage before use [27]. The predictions of the present elliptic perforation model are already within very impressive engineering tolerance.

Fig. 9 shows the α_{MPP} for the other members of the A15L50 series. The present predictions by Eq. (29) are still very accurate as the number of the micro-perforation increases, though the present model does not cater for the layout of the micro-perforations. A reduction of the sharpness of the α_{MPP} peaks and lower peak α_{MPP} values are observed as the number of perforations is increased from 49 to 121 for these A series MPPs. Though the magnitude of the perforation impedance is reduced as n_p increases (Eq. (28)), the contribution from the cavity is also affecting the z_{MPP} and thus the α_{MPP}. One should note that the sound absorption of MPP with very few perforations is not expected to be good and thus there exists a n_p which will result in optimal MPP sound absorption performance for a given combination of micro-perforation geometry, size and backing cavity length L. Eq. (28) can be used to find this optimal n_p. One can observe that the cylindrical perforation assumption does not work well. Therefore, the corresponding estimations will not be discussed further unless when necessary. The trend of the corresponding results of the A15L20 series are similar and thus they are not presented.

The increase in the MPP thickness h results in smaller bottom perforation openings relative to their front counterparts when the laser punching setting is kept unchanged, but the eccentricity of the front and bottom perforations are still similar (Table 1). Some examples of the

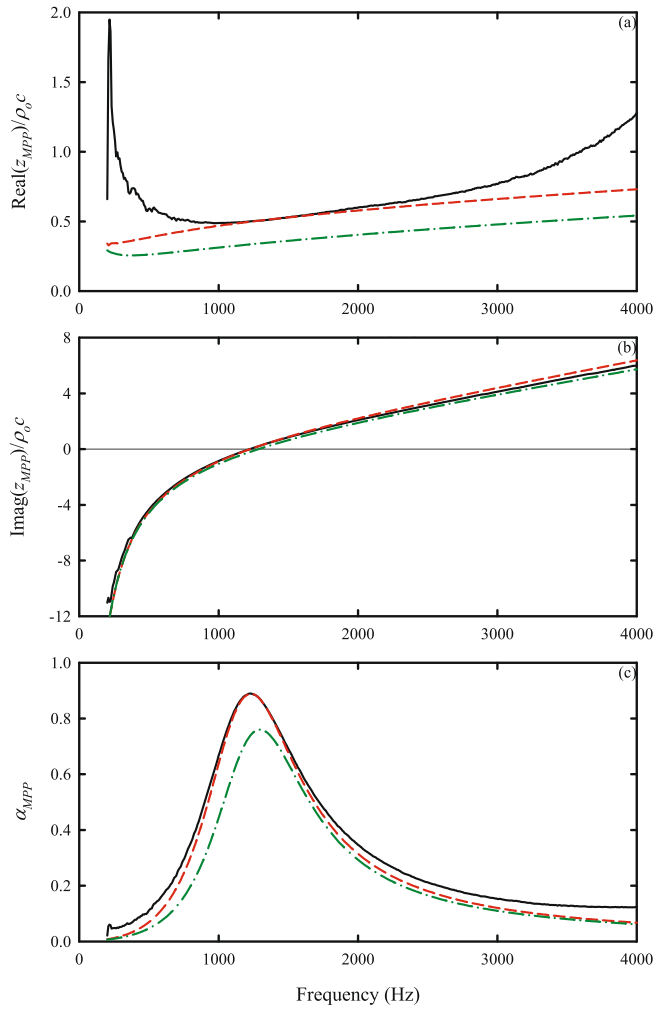

Fig. 7. Comparison between predicted specific acoustic impedances and experiments for A15L20N49S30. (a) Resistance; (b) reactance; (c) α_{MPP}. ———: Experiment; – – – –: present elliptic model; — · —: cylindrical perforation assumption.

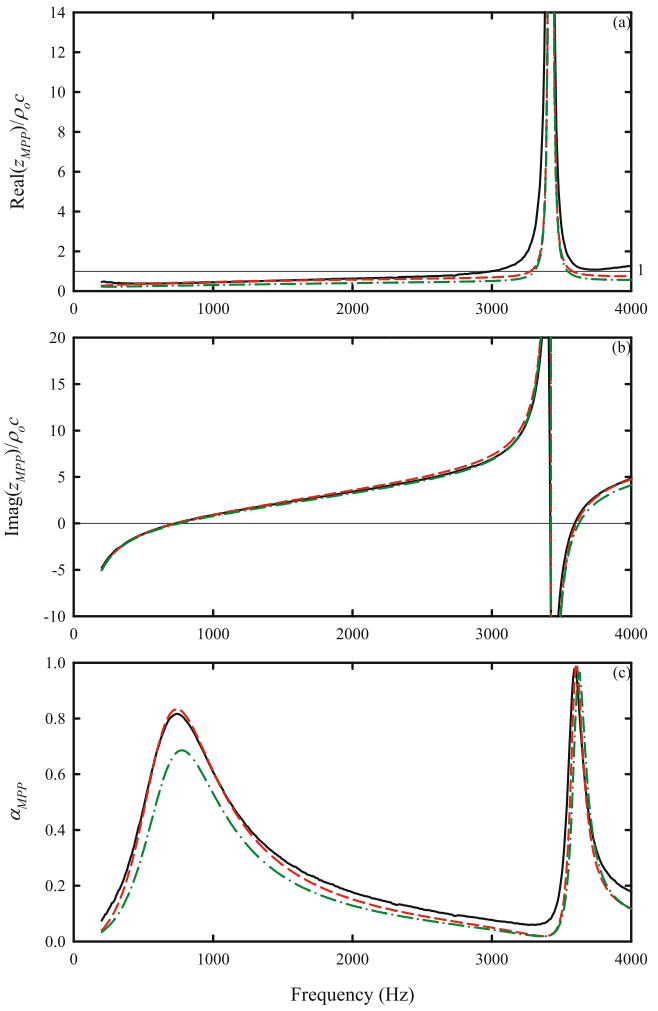

Fig. 8. Comparison between predicted specific acoustic impedances and experiments for A15L50N49S30. Legends: same as those of Fig. 7.

corresponding α_{MPP}s with $L = 50$ mm are presented in Fig. 10. The increase in h leads to higher peak α_{MPP} values. It is observed that the present elliptic model prediction becomes less accurate when h is increased to 3 mm. This can be anticipated as the perforation interior could be very different from the simple assumption made in the present study (Eq. (19)). It is expected that the thicker the MPP, the worse will be the prediction accuracy. However, a three-millimeter-thick MPP is already a very thick panel in practice.

The perforations of the B series MPP absorbers are in general smaller in size, but more cylindrical and less tapered than those of the A series absorbers. Some examples of their α_{MPP}s are presented in Fig. 11. As the perforations are more circular and less tapered, the predictions obtained by using the present elliptic model and the formula of Maa [1] are closer but the former is still better in giving the peak sound absorption frequencies as well as the absorption magnitude across most of the frequency range of the present study. Unlike the case of the A series MPP (Fig. 10), one can notice that the α_{MPP} of the B series MPP tends to decrease with increasing h (Fig. 11e and f). However, it is reduced when n_p is increased (Fig. 11d and e).

It should be noted that the predictions by the present elliptic model agree very well with experimental results even the model does not take into account the effect of the dome-like edges. This tends to imply that the smooth edges do not have significant effect on the acoustic impedance of the perforations.

4. Effects of panel thickness and eccentricity differential

It should be noted that the effects of the MPP thickness h on the sound absorption is not fully revealed in the previous sections as the size and geometry of the bottom perforation opening cannot be kept unchanged when the panel thickness is varied in the production process. Also, it is not clear how a change of the eccentricity of the bottom perforation while that of the front perforation and h are kept constant would affect the sound absorption of a MPP absorber. As the control of the elliptic perforation geometry cannot be precisely done at this moment, the above effects are examined using the present elliptic model.

Without loss of generality, the MPP A20L50N121S22 is chosen for the illustration. Fig. 12a shows the spectral variation of α_{MPP} when the panel thickness is changed to 1.5 mm and 3 mm while the geometries of the front and bottom side opening of the perforation are kept unchanged. Under this MPP configuration, both the peak α_{MPP} values and the overall sound absorption increase with increasing h. This trend remains the same when L is reduced to 20 mm and applies to other MPP configurations (not shown here). The increase in h also results in stronger perforation reactance and thus for a fixed L, the resonance of the MPP absorber and thus the sound absorption peaks appear at lower frequencies.

While it is expected that the increase in h will result in a higher perforation acoustical resistance, the higher sound absorption capacity, especially near to the peak frequencies, is due to an overall resistance (in

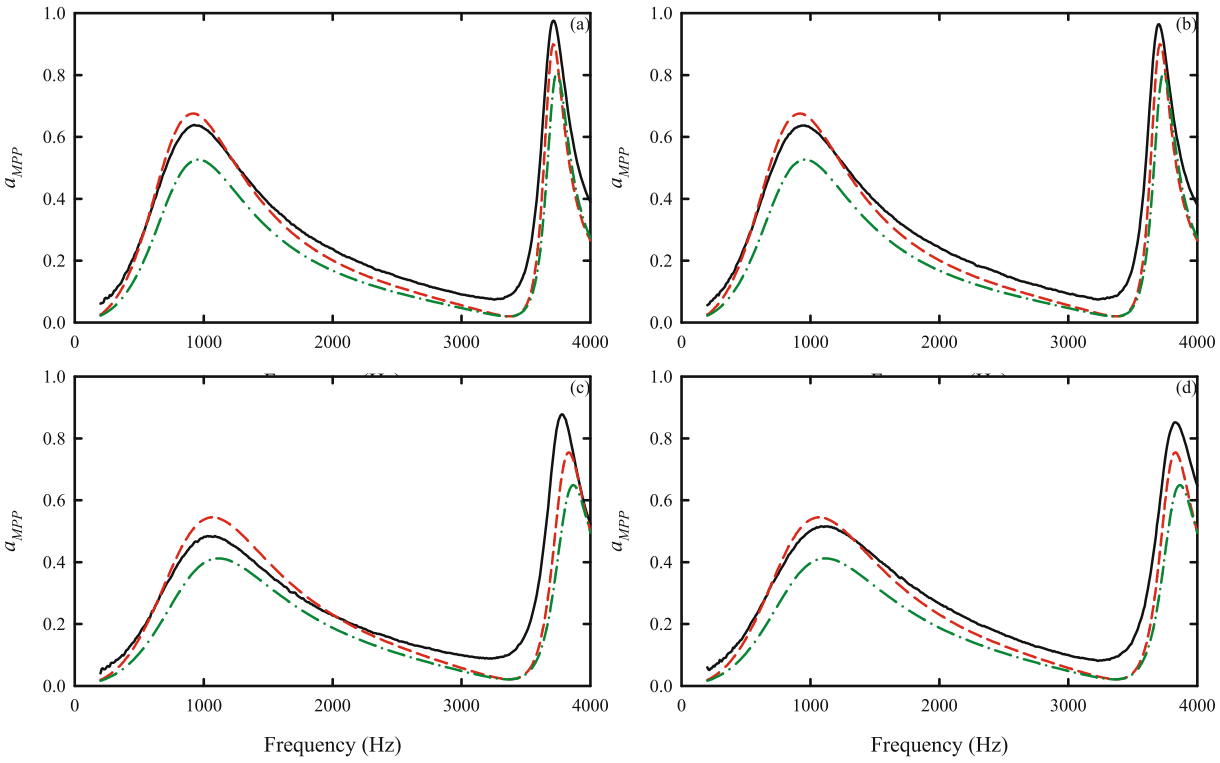

Fig. 9. α_{MPP} of the A15L50 series. (a) N81S25; (b) N81S; (c) N121S22; (d) N121S15. ———: Experiment; – – – –: present elliptic model; — · —: cylindrical perforation assumption.

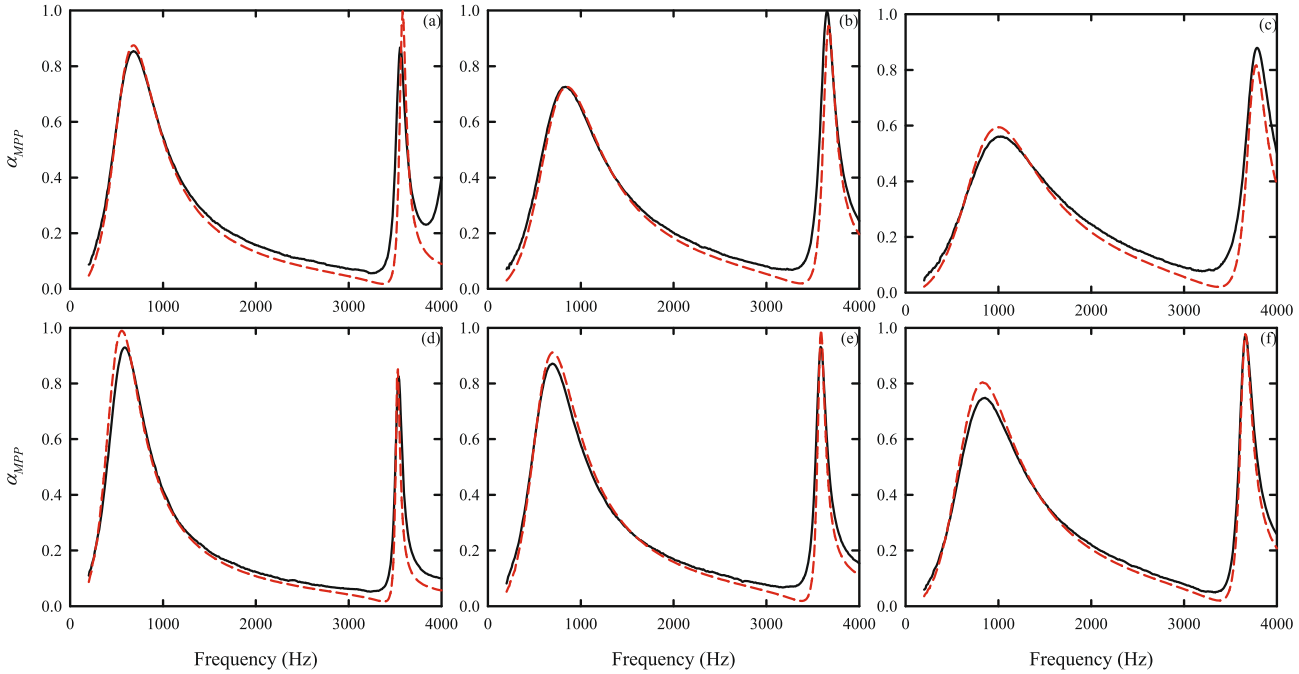

Fig. 10. Effect of MPP thickness on the prediction of α_{MPP} of the A series MPP, L = 50 mm. (a) A20L50N49S30; (b) A20L50N81S25; (c) A20L50N121S15; (d) A30L50N49S30; (e) A30L50N81S25; (f) A30L50N121S15. ———: Experiment; – – – –: present elliptic model.

z_{MPP}) closer to $\rho_o c$. As the resistance term in the cavity impedance is insignificantly small except at the very narrow resonance band at higher frequency, the first term on the right-hand-side of Eq. (28) determines the overall resistance. The number of perforations per unit area n_p thus plays a dominant role in affecting the variation of α_{MPP} with h observed in Fig.12a. For the case of A20L50N121S22, the resistance term in Z_{tap}/n_p is well below $\rho_o c$ (Fig. 12b) and thus increasing h results in an increase in α_{MPP}. One can then anticipate that this trend will be reversed for relatively small n_p where Real(Z_{tap}/n_p) is already close to $\rho_o c$ when h = 1.5 mm. For the present example, this will happen when the n_p is reduced by a factor of ~ 6.

The effect of the perforation bottom side opening eccentricity, e_b, on

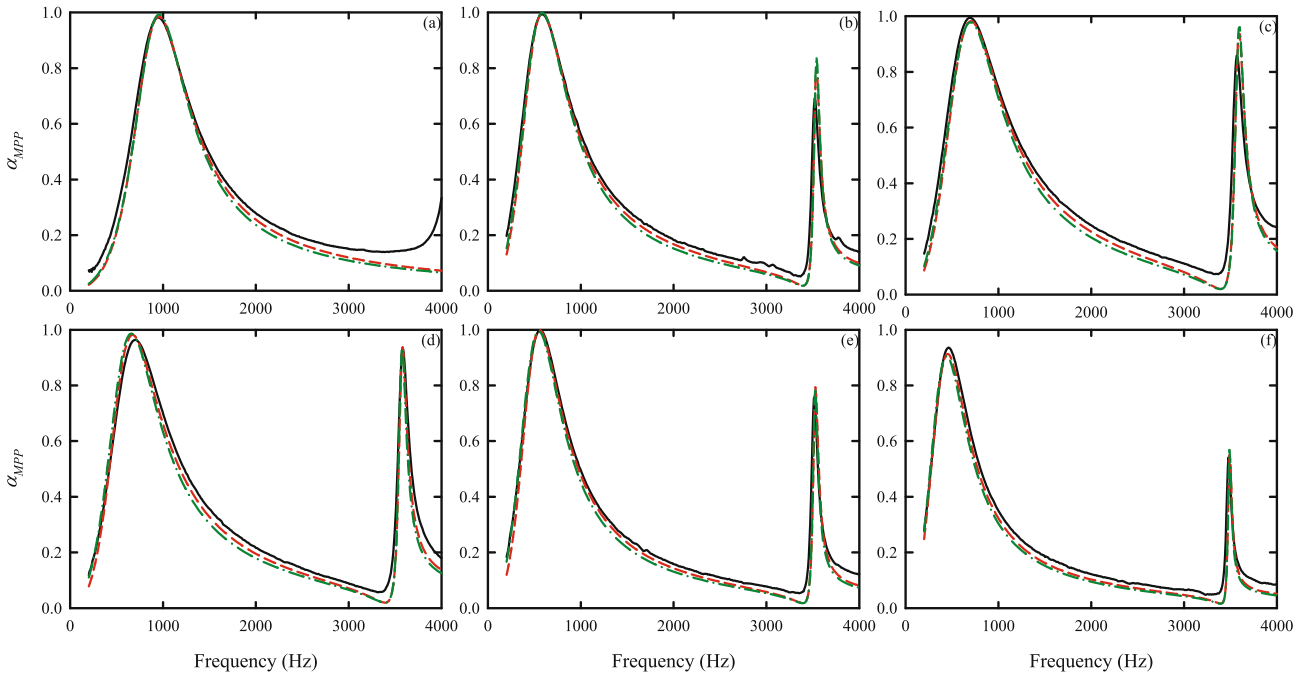

Fig. 11. Examples of α_{MPP} of the B series MPP and the accuracy of theoretical prediction. (a) B15L20N81S25; (b) B15L50N81S25; (c) B15L50N121S15; (d) B20L50N121S15; (e) B20L50N81S25; (f) B30L50N81S25. Legends: same as those of Fig. 9.

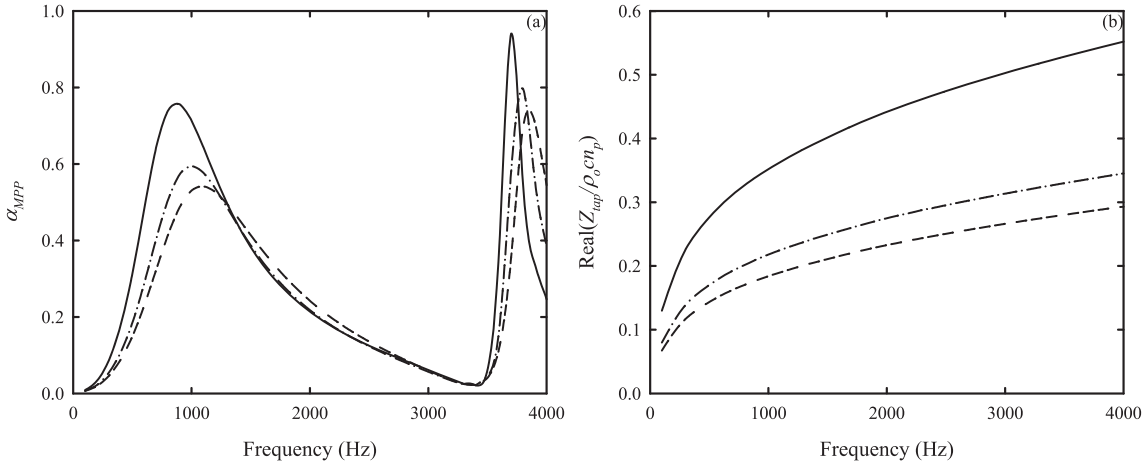

Fig. 12. Effect of panel thickness on sound absorption performance of MPP absorbers. $\alpha_f = 0.99$ mm, $\beta_f = 0.67$ mm, $\alpha_b = 0.73$ mm, $\beta_b = 0.43$ mm, $L = 50$ mm, 121 perforations, perforation separation = 2.2 mm. (a) α_{MPP}; (b) resistance of perforation — · —: $h = 1.5$ mm; − − − −: $h = 2$ mm (A20L50N121S22); ———: $h = 3$ mm.

the sound absorption characteristics of the MPP absorber is illustrated in Fig. 13a. The sound absorption capacity of the MPP absorber increases with a more elliptic bottom side opening when h, e_f, A_f and A_b are fixed. The same trend is observed when e_f is allowed to change in the same manner with a constant perforation bottom side geometry and h. The change in the eccentricities of the openings does not result in much variation in the overall reactance of the perforation. There is therefore no noticeable change in the sound absorption peak frequencies when L is fixed as shown in Fig. 13a.

The change in the eccentricity does however result in significant variation in α_{MPP}. An increase of eccentricity of either opening of the perforation improves the sound absorption capacity of the MPP absorbers because of the increase of the MPP's acoustic resistance towards the specific acoustic impedance of air (Fig. 13b). Again, this trend depends on n_p as explained before. The α_{MPP} variation trends of the other MPP absorbers are basically the same as those presented in Figs. 12 and 13. They are not presented.

5. Conclusions

A theoretical model was developed in the present study to estimate the specific acoustic impedances and the sound absorption coefficients of micro-perforated panels with tapered elliptic perforations. This type of perforations is commonly found on light-weight acrylic sound absorption panels where the tiny holes are produced by laser punching. In the model, plane wave propagation was assumed along the length of the perforation in the presence of a viscous boundary layer at the perforation internal wall surface. Structural vibration and damping were not considered in the present study as these effects depend on the actual size of the absorber panel, which varies widely in practical applications.

Experimental validation has been carried out using standard impedance tube method. Diameters of the test specimen were fixed at 29 mm, while their thickness varied from 1.5 mm to 3 mm. Micro-perforated acrylic panels with different perforation geometries, separations and layouts were included in the validation. Comparison with

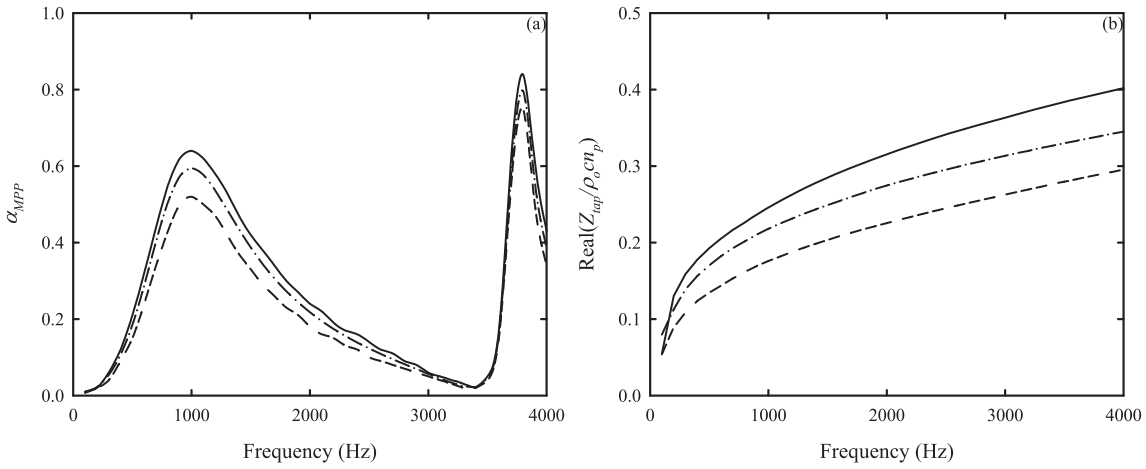

Fig. 13. Effect of eccentricity differential on sound absorption performance of MPP absorbers. $\alpha_f = 0.99$ mm, $\beta_f = 0.67$ mm, $L = 50$ mm, $h = 2$ mm, 121 perforations, perforation separation = 2.2 mm. (a) α_{MPP}; (b) resistance of perforation — · —: $e_b = 0$; – – – –: $e_b = 0.81$ (A20L50N121S22); ———: $e_b = 0.90$.

the predictions by conventional cylindrical perforation model was also presented.

Results show that the present model gives much more accurate predictions than the conventional cylindrical perforation model, especially around the peak sound absorption frequencies for more elliptic perforation (eccentricity ~ 0.7). The prediction error increases with panel thickness but is still very much within engineering tolerance for a 3 mm thick panel. The predictions of the present model and the conventional cylindrical perforation model are closer when the perforations become more cylindrical and less tapered. However, the present model still produces more accurate results, in term of both the peak sound absorption frequencies as well as the sound absorption coefficients within the frequency range of the present study.

The present elliptic perforation model also suggests that there exists a critical perforation density above which the sound absorption capacity of a MPP absorber will be improved if the panel thickness is increased with constant perforation opening geometries. Similar observation applies when a more elliptic perforation opening is adopted.

CRediT authorship contribution statement

M.L. Fung: Investigation, Software, Methodology, Validation, Formal analysis, Data curation, Writing – original draft, Visualization. **S. K. Tang:** Conceptualization, Methodology, Formal analysis, Resources, Data curation, Writing – review & editing, Supervision, Project administration, Funding acquisition. **M. Leung:** Funding acquisition, Writing – review & editing, Resources, Methodology.

Declaration of Competing Interest

The authors declare that they have no known competing financial interests or personal relationships that could have appeared to influence the work reported in this paper.

Data availability

Data will be made available on request.

Acknowledgments

The financial supported from the Innovation and Technology Commission, The Hong Kong Special Administration Region Government, China under Project number UIM/360 is gratefully acknowledged.

References

[1] Maa DY. Theory and design of microperfored panel sound-absorbing constructions. Sci Sin 1975;18(1):55–71.
[2] Maa DY. Potential of microperforated panel absorber. J Acoust Soc Am 1998; 104 (5): 2861 – 6.
[3] Harris CM. Handbook of Noise Control. New York: McGraw-Hill; 1979.
[4] Fuch HV, Zha X. Micro perforated structures as sound absorbers – A review and outlook. Acta Acust United Acust 2006;92(1):139–46.
[5] Liu J, Hua X, Herrin DW. Estimation of effective parameters for micro-perforated panel absorbers and application. Appl Acoust 2014;75:86–93.
[6] Bravo T, Maury C, Pinhède C. Sound absorption and transmission through flexible micro-perforated panels backed by an air layer and a thin plate. J Acoust Soc Am 2012; 131(5): 3853 – 63.
[7] Sakagami K, Morimoto M, Yairi M, Minemura A. A pilot study on improving the absorptivity of a thick microperforated panel absorber. Appl Acoust 2008;69(2): 179–82.
[8] Sakagami K, Nakamori T, Morimoto M, Yairi M. Double-leaf microperforated panel space absorbers: A revised theory and analysis. Appl Acoust 2009;70(5):703–9.
[9] Bravo T, Maury C, Pinhède C. Enhancing sound absorption and transmission through flexible multi-layer micro-perforated structures. J Acoust Soc Am 2013; 134(5): 3663 – 73.
[10] Cobo P, Simón F. Multiple-layer microperforated panels as sound absorbers in buildings: a review. Buildings 2019;9(2):53.
[11] Wang C, Cheng L, Pan J, Yu G. Sound absorption of a micro-perforated panel backed by irregular-shaped cavity. J Acoust Soc Am 2010;127(1):238–46.
[12] Wang CQ, Huang L. On the acoustic properties of parallel arrangement of multiple microperforated panel absorbers with different cavity depths. J Acoust Soc Am 2011; 130(1): 208 – 18.
[13] Allam S, Åbom M. A new type of muffler based on microperforated tubes. ASME Trans J Vib Acoust 2011;133(3):031005.
[14] Xi Q, Choy YS, Cheng L, Tang SK. Noise control of dipole source by using micro-perforated panel housing. J Sound Vib 2016;362:39–55.
[15] Gao N, Zhang Z, Deng J, Guo X, Cheng B, Hou H. Acoustic metamaterials for noise reduction: A review. Sci Rep 2017;7(1):2100698.
[16] Stinson MR. The propagation of plane sound waves in narrow and wide circular tubes, and generalization to uniform tubes of arbitrary cross-sectional shape. J Acoust Soc Am 1991; 89(2) 550 – 8.
[17] Ning JF, Ren SW, Zhao GP. Acoustic properties of micro-perforated panel absorber having arbitrary cross-sectional perforations. Appl Acoust 2016;111:135–42.
[18] Tang SK. On Helmholtz resonators with tapered necks. J Sound Vib 2005;279(3–5): 1085–96.
[19] Herdtle T, Bolton JS, Kim NN, Alexander JH, Gerdes RW. Transfer impedance of microperforated materials with tapered holes. J Acoust Soc Am 2013; 134(6): 4752 – 62.
[20] Rayleigh JWS. The Theory of Sound Vol. II, 2nd Ed. New York; Dover: 1945.
[21] Abramowitz M, Stegun IA. Handbook of Mathematical Functions with Formulas, Graphs, and Mathematical Tables. New York: Dover; 1970.
[22] Acoustics Module User's Guide. COMSOL Multiphysics; 2018.
[23] Ingard U. On the theory and design of acoustic resonators. J Acoust Soc Am 1953; 25(6): 1037 – 61.
[24] Abbott P. On the perimeter of an ellipse. Math J 2009;11(2):4.
[25] Nielsen AK. Acoustic resonators of circular cross-section and with axial symmetry. Trans Dan Acad Techn Sci 1949:10.
[26] Mechel FP. Formulas of Acoustics 2nd Ed. New York: Springer; 2008.
[27] Takahashi D, Tanaka M. Flexural vibration of perforated plates and porous elastic materials under acoustic loading. J Acoust Soc Am 2002; 112(4): 1456 – 64.